Bioactive Materials 19 (2023) 103–114

Contents lists available at ScienceDirect

Bioactive Materials

journal homepage: www.keaipublishing.com/en/journals/bioactive-materials

Bone without borders – Monetite-based calcium phosphate guides bone formation beyond the skeletal envelope

Furqan A. Shah [a,*], Martina Jolic [a], Chiara Micheletti [a,b], Omar Omar [a], Birgitta Norlindh [a], Lena Emanuelsson [a], Håkan Engqvist [c], Thomas Engstrand [d], Anders Palmquist [a], Peter Thomsen [a]

[a] Department of Biomaterials, Sahlgrenska Academy, University of Gothenburg, Gothenburg, Sweden
[b] Department of Materials Science and Engineering, McMaster University, Hamilton, Ontario, Canada
[c] Department of Engineering Sciences, Applied Materials Science Section, Uppsala University, Uppsala, Sweden
[d] Department of Reconstructive Plastic Surgery, Karolinska University Hospital, Stockholm, Sweden

ARTICLE INFO

Keywords:
Bone
Calcium phosphate
Monetite
Calcium pyrophosphate
Electron microscopy
Raman spectroscopy

ABSTRACT

Calcium phosphates (CaP) represent an important class of osteoconductive and osteoinductive biomaterials. As proof-of-concept, we show how a multi-component CaP formulation (monetite, beta-tricalcium phosphate, and calcium pyrophosphate) guides osteogenesis beyond the physiological envelope. In a sheep model, hollow dome-shaped constructs were placed directly over the occipital bone. At 12 months, large amounts of bone (~75%) occupy the hollow space with strong evidence of ongoing remodelling. Features of both compact bone (osteonal/osteon-like arrangements) and spongy bone (trabeculae separated by marrow cavities) reveal insights into function/need-driven microstructural adaptation. Pores within the CaP also contain both woven bone and vascularised lamellar bone. Osteoclasts actively contribute to CaP degradation/removal. Of the constituent phases, only calcium pyrophosphate persists within osseous (cutting cones) and non-osseous (macrophages) sites. From a translational perspective, this multi-component CaP opens up exciting new avenues for osteotomy-free and minimally-invasive repair of large bone defects and augmentation of the dental alveolar ridge.

1. Introduction

Bone forms by differentiation of osteoprogenitor cells into either mesenchymal osteoblasts that synthesise disordered woven bone or surface osteoblasts that produce highly ordered lamellar bone [1]. Classically considered a feature of foetal bone development, recent evidence suggests that endochondral and intramembranous ossifications also occur postnatally, particularly during skeletal regeneration in the event of injury [2]. In fracture healing, bone recapitulates foetal bone development to achieve complete tissue regeneration without forming a fibrous scar [3]. In this process several transitional tissue types including fibrous callus, scarcely-mineralised cartilage, and woven bone are involved depending on the extent of mechanical stimuli [4,5]. These intermediate tissue types provide initial mechanical stability and are eventually replaced by ordered lamellar bone [5]. While bone has an intrinsic capacity for regeneration and healing [6] and continually undergoes remodelling [7], incomplete or irregular postnatal osteogenesis can still occur in large bone defects. Failure of regeneration can be caused by substantial injuries, tumour resections, skeletal abnormalities, infections, or systematic disorders such as osteoporosis [8].

Controlled, on demand, and complete bone formation is a long coveted *holy grail* of bone tissue engineering. Currently, the 'gold standard' for bone augmentation are autologous bone grafts. Commonly used in orthopaedic and maxillofacial surgery, they provide great histocompatibility and structural support, and present a minimal risk of immunogenic response [9]. However, major challenges such as increased operating time, limited availability, and risk of donor site morbidity [10] have driven the development of synthetic bone graft substitutes [8].

Skeletal tissue regeneration achieved by combining pre-expanded cells and growth factors with an appropriate scaffold is a promising approach, however, synthetic bone graft substitutes with inherent osteoinductive properties may offer a more comprehensive solution [11]. A wide range of biomaterials are currently used as scaffolds [10]. Calcium phosphate (CaP) based materials are among the most commonly used bone graft substitutes [12]. Synthetic CaPs possess

Peer review under responsibility of KeAi Communications Co., Ltd.
* Corresponding author.
E-mail address: furqan.ali.shah@biomaterials.gu.se (F.A. Shah).

https://doi.org/10.1016/j.bioactmat.2022.03.012
Received 16 November 2021; Received in revised form 2 March 2022; Accepted 7 March 2022

several desirable characteristics including protein adhesion, *in vivo* degradation, bone-bonding ability, and osteoconductivity [13]. Additionally, osteoinductivity may be achieved via a macroporous 3D environment [14].

Membranes for guided bone regeneration, a prime example of space-maintaining devices, are used clinically in the oro-maxillo-facial region to achieve increased horizontal/lateral bone regeneration [15]. Although the majority of clinically used non-resorbable and resorbable membranes are synthetic polymers and collagen, membranes consisting of hydroxy(l)apatite or CaP-containing composite materials have yielded interesting bone regenerative effects in subperiosteal bone defects [16]. Nevertheless, previous attempts at supraperiosteal bone apposition (or augmentation) using hollow, dome-shaped constructs made of hydroxy(l)apatite have shown limited success [17]. Multi-component calcium phosphate (CaP) compositions containing predominantly monetite ($CaHPO_4$) with smaller additions of beta-tricalcium phosphate (β-$Ca_3(PO_4)_2$, β-TCP) and calcium pyrophosphate ($Ca_2P_2O_7$, Ca-PP) exhibit osteoinductive behaviour [18] and long-term volumetric balance between rates of bone formation and CaP degradation [19]. Although the osteoinductive properties of monetite-containing materials [20], including bone repair cements [21], and β- TCP [22] are reported, the precise role and eventual fate of Ca-PP warrants further investigation. Pyrophosphate ions ($P_2O_7^{4-}$) act as inhibitors of calcification and actively prevent pathological mineralisation [23]. *In vitro*, pyrophosphate ions can bind directly to active sites on the mineral and prevent further crystal growth, inhibit production of free phosphate from organic molecules such as beta-glycerol phosphate, and upregulate the expression of inhibitory proteins [24,25]. Ca-PP is also implicated in stimulation of osteogenic differentiation and mineralisation through upregulated expression and enzymatic activity of alkaline phosphatase (ALP), thereby increasing local concentrations of Ca^{2+} and PO_4^{3-} upon cleavage by ALP [26–28]. *In vivo*, Ca-PP supports bone formation across the surface and progressively degrades [29]. Moreover, degradable bone repair cements containing Ca-PP retain osteoconductive properties without interfering with mineralisation of healing bone [30].

Here, we demonstrate the efficacy of a multi-component CaP containing monetite, β-TCP, and Ca-PP obtained in the form of a dome-shaped hollow construct, to guide bone regeneration beyond the physical confines of the skeletal envelope. Furthermore, we undertake a comprehensive investigation of how such extraskeletal bone (EB) compares with the underlying native bone (NB) in terms of composition and microarchitecture (Table S1), and whether it possesses the capacity to undergo remodelling and/or the potential to sense mechanical loading.

2. Materials and methods

A multi-component calcium phosphate (CaP) formulation was fabricated in the form of a dome-shaped construct with an integrated Ti6Al4V frame consisting of two vertically-offset rings (~1 mm strut thickness) and two lateral loops for screw placement. Seven such constructs were investigated for their potential to guide osteogenesis into the dome-shaped hollow space using an occipital bone model in adult female sheep (*Ovis aries*). After 52 weeks *in vivo*, all of the constructs were retrieved together with associated bone and processed for subsequent characterisation of bone quality.

Multi-component CaP fabrication. The multi-component CaP was prepared using a mixture of beta-tricalcium phosphate [β-$Ca_3(PO_4)_2$, β-TCP; Sigma-Aldrich] containing dicalcium pyrophosphate [$Ca_2P_2O_7$, Ca-PP] as an impurity and monocalcium phosphate monohydrate [$Ca(H_2PO_4)_2.H_2O$; Alfa Aesar, Thermo Fisher] powders, at a mass ratio of 55:45, with glycerol (Sigma-Aldrich), at a powder-to-liquid ratio of 3.9 g/mL. A 3D printed Ti6Al4V ELI frame was positioned into a dome-shaped mould (15 mm in diameter and 4 mm in height). The CaP and glycerol paste was poured over the frame and allowed to set overnight in sterile water. After removal from the mould, the construct was left in sterile water for 48 h to eliminate glycerol and rendered hollow using a 2 mm diameter rotary drill. The final thickness of the intact CaP (i.e., as-manufactured) was ~2 mm. Surface morphology of intact CaP was evaluated using a Nikon SMZ1500 stereomicroscope (Nikon Ltd., Tokyo, Japan) equipped with an HR Plan Apo 1× objective lens.

***In vivo* implantation, retrieval, and specimen processing.** Ti6Al4V reinforced, dome-shaped hollow CaP constructs were investigated *in vivo*, in the absence of potential stimulatory effect(s) of mechanical (physiological or functional) loading in adult female sheep ($n = 7$). Under anaesthesia, a flap was elevated by blunt dissection in the subperiosteal plane. In each sheep, one construct was placed directly over the occipital bone (without any surface preparation of the recipient bone such as roughening, drilling, or decortication) and stabilised, via the lateral loops, using two osteosynthesis screws. After 52 weeks, the multi-component CaP constructs and associated extraskeletal bone (EB) were dissected along with the underlying native bone (NB), fixed in 10% neutral buffered formalin, and resin embedded (LR White, London Resin Co. Ltd., UK). The animal experiment was approved by the Ministry of National Education, Higher Education and Research (NAMSA, Chasse-sur-Rhône, France; Approval nr. 01139.2).

X-ray diffraction. Phase composition of intact CaP (~84.7% monetite, ~8.3% β-TCP, and 6.8% Ca-PP) was analysed using X-ray diffraction (XRD, Bruker D8 Advance X-ray diffractometer, Billerica, MA, USA) over an angular range of 20°–45° 2θ at a step size of 0.03° using Cu-Kα radiation and Rietveld refinement, as described previously [18].

X-ray micro-computed tomography. Resin embedded CaP-bone blocks were evaluated using X-ray micro-computed tomography (micro-CT). All samples were scanned over a 180° rotation at a step size of 0.5° with an average of four frames and an image pixel size of 13.90 μm in a Skyscan 1172 (Bruker micro-CT, Kontich, Belgium) operated at 49 kV energy with an Al filter (0.5 mm). BMD calibration phantoms (0.25 g/cm^3 and 0.75 g/cm^3 stoichiometric hydroxyapatite in epoxy resin, 2 mm diameter) were also scanned using the same settings. Visualisation of micro-CT datasets and quantitative analysis were carried out using Dragonfly (v. 2020.1, Objects Research Systems, QC, Canada). As the two main regions of interest (ROI), bone within the dome-shaped hollow space (excluding bone inclusions within the CaP bulk) was considered EB and segmented using the *ROI Painter* freehand tool in a few representative *x-y* slices and then interpolated in the *z* direction. A cuboid region of the native cortical bone immediately underlying EB (such that the total volume was within ±10% of the total volume of the corresponding EB) was taken as NB. For quantification of bone volume fraction (BV/TV), the bone volume (BV) of each ROI was segmented based on greyscale intensity using the *Range* tool. To obtain the total volume (TV), porosities attributed to unmineralised/non-bone areas (i.e., blood vessels and marrow cavities) in each ROI were filled using the "fill inner areas" operation. BV/TV was computed by dividing the volume occupied by bone (BV) within the selected ROI by the total volume of the ROI (i.e., bone with filled pores, TV). Non-osseous pore size was measured using the "create volume thickness map" operation, which involves inscribing spheres of maximal possible diameters within the 3D features in the foreground.

Scanning electron microscopy. Samples of intact CaP were Au sputter-coated (~10 nm) for secondary electron scanning electron microscopy (SE-SEM) in an Ultra 55 FEG SEM (Leo Electron Microscopy Ltd, UK) operated at 5 kV accelerating voltage. Additionally, samples of intact CaP were resin embedded (LR White, London Resin Co. Ltd., UK), polished using 400–4000 grit SiC paper and absolute ethanol for back-scattered electron scanning electron microscopy (BSE-SEM) in a Quanta 200 environmental SEM (FEI Company, The Netherlands) operated at 20 kV accelerating voltage, 1 Torr water vapour pressure, and 10 mm working distance. Resin embedded CaP-bone (52 w CaP) blocks were polished using 400–4000 grit SiC paper and absolute ethanol. For enhanced contrast of unmineralised/soft tissue, a stock solution of iodine in potassium iodide (Lugol solution, I_2/KI, Sigma-Aldrich) was diluted 1:1 in ethanol, and pipetted (~150–200 μL) directly onto

polished resin embedded blocks for ~15 min. The stain was washed off with deionised water. BSE-SEM was performed with and without I_2/KI staining in a Quanta 200 environmental SEM (FEI Company, The Netherlands) operated at 20 kV accelerating voltage, 1 Torr water vapour pressure, and 10 mm working distance.

Elemental analysis. Resin embedded/polished intact CaP and resin embedded/polished CaP-bone blocks were used for energy dispersive X-ray spectroscopy. Point-analysis was performed at 20 kV accelerating voltage and 1 Torr water vapour pressure in a Quanta 200 environmental SEM (FEI Company, The Netherlands). Ca/P ratios were calculated and Mg content was estimated as the difference between (Ca + Mg)/P and Ca/P ratios.

Histology. Undecalcified, toluidine blue and Van Gieson stained ground sections (~40 μm thick) were prepared from resin embedded CaP-bone blocks. Areas where collagen is present stain positively for Van Gieson's stain and therefore collagenous and non-collagenous sites can be readily distinguished. Brightfield imaging was performed using a Nikon Eclipse E600 optical microscope (Nikon Ltd., Tokyo, Japan) equipped with 20×, 40×, and 60× (water-immersion) objectives. ROIs containing (*i*) woven bone, (*ii*) lamellar bone, and (*iii*) a remodelling site or vascular space were identified using a 20× objective. Woven and lamellar bone areas were manually demarcated using ImageJ (*imagej.nih.gov/ij*). Epifluorescence microscopy was performed using a 465–495 nm excitation filter and a 515–555 nm emission filter. Polarised light microscopy (PLM) was performed using a Zeiss Axio Imager.Z2 (Zeiss, Oberkochen, Germany) equipped with an EC Plan-Neofluar 10×/0.3 NA objective.

Transmission electron microscopy (TEM). From one resin embedded CaP-bone block, two electron-transparent samples were prepared using the focussed ion beam (FIB) *in situ* lift-out technique on a Versa 3D Dualbeam (FEI Company, The Netherlands) FIB/SEM. High-angle annular dark-field scanning transmission electron microscopy (HAADF-STEM) was used for *Z*- (atomic number) contrast imaging in a Tecnai F20 microscope (FEI Company, The Netherlands) operated at 200 kV.

Fourier transform infrared spectroscopy. Spectra were obtained with a Fourier transform infrared microscope (FTIR, HYPERION 3000, Bruker Optics, Billerica, MA, USA) in reflectance mode coupled with a spectrometer (VERTEX 70v FTIR spectrometer with nitrogen cooled mercury cadmium telluride detector, Bruker Optics, Billerica, MA, USA). Resin embedded/polished CaP-bone blocks were placed on the motorised stage and measurements were obtained with a Germanium ATR objective (20×) at the lowest pressure point setting between the sample and the Ge crystal during spectral acquisition. Measurement parameters were set to a step size of 1.93 cm^{-1}. 64 scans were averaged to achieve a good signal-to-noise ratio. Measurement points were excluded where signal intensity was low owing to poor contact between the ATR crystal and the sample surface.

Micro-Raman spectroscopy. Micro-Raman spectroscopy was performed using a confocal Raman microscope (Renishaw inVia Qontor, Renishaw plc. Wotton under Edge, UK) equipped with a 633 nm laser and LiveTrack focus-tracking technology, which enables enhanced signal stability at non-planar and non-plane parallel surfaces [31]. The laser was focussed down on to the surface of intact CaP, resin embedded/polished intact CaP, resin embedded/polished CaP-bone (52 w CaP) blocks using a 100×/0.9 NA objective [32]. The Raman scattered light was collected using a Peltier-cooled charge-coupled device deep depletion near-infrared enhanced detector behind an 1800 g mm^{-1} grating (1.0 ± 0.15 cm^{-1} step size) or a 2400 g mm^{-1} (0.75 ± 0.04 cm^{-1} step size) grating. The laser power at the sample was ~15 mW. Baseline subtraction and cosmic ray removal were performed in Renishaw WiRE 5.4 software. Integral area maps for CHAp (940–980 cm^{-1}), Amide III (1210–1290 cm^{-1}), monetite (890–910 cm^{-1}), β-TCP (970–972 cm^{-1}), Ca-PP (1042–1051 cm^{-1}), and PMMA (600–606 cm^{-1}) were generated.

Resin cast etching. For direct visualisation of the osteocyte lacunocanalicular network using resin cast etching (RCE), resin embedded/polished CaP-bone blocks were immersed in 9% H_3PO_4 (for 30 s), rinsed in Milli-Q water (for 5 s), immersed in 10% NaOCl (for 5 min), rinsed again (for 30 s), and air-dried overnight. The samples were Au sputter-coated (~10 nm) for high vacuum SE-SEM imaging in an Ultra 55 FEG SEM (Leo Electron Microscopy Ltd, UK) operated at 5 kV.

Statistical analysis. The Mann-Whitney *U* test was used for elemental analysis with energy dispersive X-ray spectroscopy. The Wilcoxon signed-rank test was used for all comparisons between EB and NB, in a pair-wise manner. Linear regression analysis was used for size (2D area) vs. aspect ratio of marquise-shaped motifs at regions of ongoing mineralisation. Mean values ± standard deviations are presented and p values < 0.05 were considered statistically significant.

3. Results

3.1. Multi-component CaP transforms to carbonated apatite after 52 weeks in vivo

The surface of intact CaP (i.e., as manufactured) is heterogeneous (Fig. 1 A) and is characterised by a combination of thin platelet-like crystals, facetted polygonal crystals, and smooth/rounded particles (Fig. 1 B–C). Throughout the bulk of intact CaP, in addition to large pores often reaching up to ~200 μm in diameter, the CaP matrix exhibits variable local density (Fig. 1 D–F). Elemental composition determined using energy dispersive X-ray spectroscopy indicates a noteworthy increase ($p < 0.001$) in the Ca/P ratio from ~0.86 ± 0.02 at% of intact CaP to ~1.20 ± 0.1 at% after 52 weeks *in vivo*. Mg enrichment is also noted ($p < 0.001$) from 0.4 ± 0.2 at% of intact CaP to 3.4 ± 1.5 at% at 52 weeks *in vivo* (Fig. 1 G). Powder X-ray diffraction confirms the various constituent phases present in the intact CaP (Fig. 1 H). Real-time surface tracked micro-Raman spectroscopy enabled mapping the phase composition of intact CaP without mechanically rendering the surface planar (e.g., by polishing) or excluding topological irregularities [31]. All the characteristic spectral features of monetite (at ~900 and ~986 cm^{-1}), β-TCP (at ~947 cm^{-1} and ~970–972 cm^{-1}), and Ca-PP (at ~1043–1048 cm^{-1}) are identified [33] (Fig. 1 I, Fig. S1). After 52 weeks *in vivo*, physical degradation and chemical transformation are evident within the CaP bulk. The multi-component CaP partially transforms to carbonated apatite (CHAp, peak at ~959–962 cm^{-1}) primarily at the expense of monetite and Ca-PP, whereas spectral features attributable to β-TCP remain detectable.

3.2. Extraskeletal bone occupies over 75% of the dome-shaped hollow space

After surgical insertion, the dome-shaped construct was held in position atop the occipital bone with fixation screws and excised after 52 weeks together with associated bone (Fig. 2 A, Fig. S2). Beyond the confines of the skeletal envelope, extraskeletal bone (EB) within the dome-shaped hollow space below the CaP occupies a major proportion of the available volume (BV/TV of 75 ± 11%) with a large non-osseous pore diameter (643 ± 332 μm) (Fig. 2 B–D). Immediately underlying EB, the native bone (NB) is comparatively denser ($p = 0.018$) and exhibits microarchitecture reminiscent of cortical/compact bone (BV/TV of 92 ± 5%), while the diameter of non-osseous pores (375 ± 187 μm) is much smaller ($p = 0.018$). Microstructure of EB tends to vary at different vertical levels within the dome-shaped hollow space (Fig. 2 E), such that along an axial plane closer to the EB–NB junction, higher porosity and architecture bearing a greater resemblance to trabecular bone are noted. Physical degradation of the CaP is apparent. Bone infiltration restricts complete disintegration of the CaP and large segments remain bridged together (Fig. 2 F–G).

Histologically, EB microstructure largely resembles that of lamellar bone (Fig. 2 F–G, Fig. S3), where immediately adjacent to the CaP surface, a pattern of concentric lamellae demonstrates osteonal architecture achieved through remodelling (Fig. 2 H). At the same time, the largest

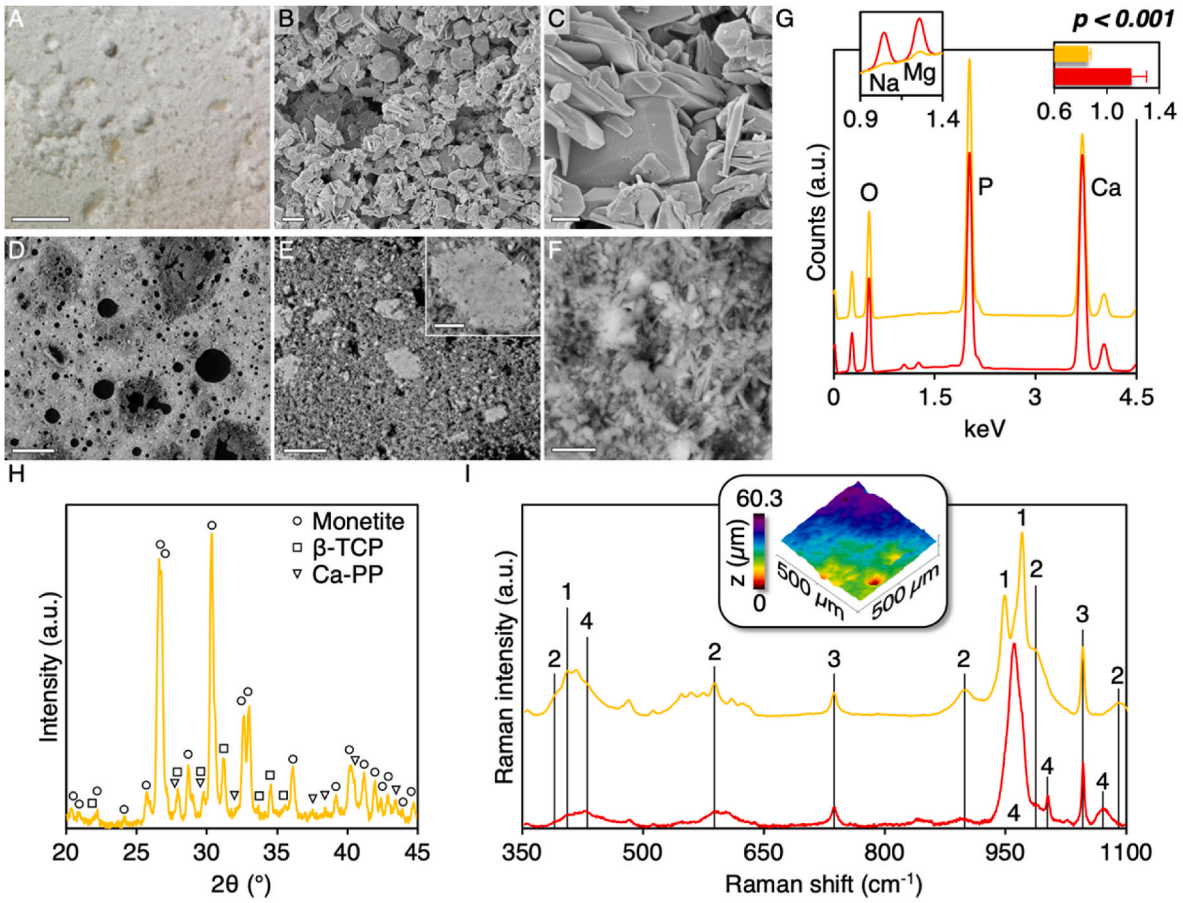

Fig. 1. Multi-component CaP microstructure and composition. A: Intact CaP surface (optical microscopy). B–C: Intact CaP surface (SE-SEM). D–F: Resin embedded/polished intact CaP (BSE-SEM). Inset in E: Ca-PP particle (Scale bar = 5 μm). G: Elemental analysis (energy dispersive X-ray spectroscopy). Left inset: Detail of the 0.9–1.4 keV range. Kα X-ray emission lines for sodium (Na, ~1.04 keV) and magnesium (Mg, ~1.253 keV) are shown. Right inset: Ca/P at% ratios of intact CaP (yellow; $n = 60$) and 52 w CaP (red; $n = 60$). Mann-Whitney U test. H: Intact CaP composition (X-ray diffraction). I: Micro-Raman spectroscopy. Intact CaP (yellow; 2500 spectra). 52 w CaP (red; 418 spectra). 1 = β-TCP; 2 = Monetite; 3 = Ca-PP; 4 = CHAp. Inset: Intact CaP surface height deviation map using LiveTrack. Scale bars in A = 500 μm, B = 2 μm, C = 500 nm, D = 200 μm, E = 20 μm, F = 2 μm. (For interpretation of the references to colour in this figure legend, the reader is referred to the Web version of this article.)

non-osseous pores in EB are occupied by bone marrow, which is usually composed of hematopoietic cells, adipose tissue, and mesenchymal stem cells that differentiate into various cell types including osteoblasts and chondrocytes [34], and is a key feature of trabecular bone. Not infrequently, osteon-like concentric arrangements of lamellar bone enclosing a central vascular canal are surrounded by yet unremodelled woven bone. BSE-SEM, with and without staining with Lugol's solution [35], reveals large variations in mineral content and distribution of osteocyte lacunae between lamellar bone and woven bone areas (Fig. S4). More prevalent in the superior half of the dome-shaped hollow space, irregularly-shaped CaP islands are also found embedded within EB and bordered by multiple (≥3) distinct packets of bone (Fig. S5). In this manner, a spatially recurring sequence emerges along the direction from the hollow space towards (and into) the CaP bulk, where lamellar bone is sandwiched between regions of woven bone. Small inclusions (<100 μm in diameter) of *de novo* bone within the CaP bulk also exhibit the characteristic disorganised appearance of woven bone, lacking the typical birefringence of lamellar bone observed using PLM (Fig. 2 I–J, Fig. S6). While the periphery of such inclusions (i.e., bone-CaP interface) tends to be jagged, there is absence of a defined vascular canal. The bone-CaP interface is more clearly demarcated where signs of bone remodelling are evident, characterised by a highly organised lamellar architecture complete with the presence of vasculature, and a gently scalloped interface comparable to Howship's lacunae in bone (Fig. S7). Endochondral-like osteogenesis is noted almost exclusively furthest from NB, e.g., in gaps created upon CaP degradation adjacent to the Ti6Al4V frame. Correlative application of BSE-SEM and RCE demonstrates the presence of osteocytes embedded within cartilage-like areas (Fig. 2 K).

Using the FIB *in situ* lift-out technique (Fig. S8), samples were obtained for HAADF-STEM. At the ultrastructural level (Fig. 2 L–O, Fig. S9), remodelled regions of EB display the characteristic ~67 nm cross-striated pattern of mineralised collagen fibrils, where oriented parallel to the image plane. Collagen fibrils assemble into a network of rope-like mineralised bundles (1–2 μm in diameter). Where collagen fibrils are oriented perpendicular to the image plane (i.e., viewed in cross-section), the rope-like mineralised bundles appear in the form of '*rosettes*' (or rosette-like clusters of fibrils) [36].

3.3. Areas of ongoing mineralisation show a characteristic granular appearance

Adjacent to recently remodelled sites in EB immediately below the CaP (Fig. 3 A–B) and within the CaP (Fig. S10), areas of ongoing mineralisation stain intensely with blue cationic dyes owing to relatively higher content of acid phosphate (HPO_4^{2-}) groups, and exhibit a granular appearance consistent with woven bone [37]. On closer inspection, discrete, marquise-shaped motifs are observed (Fig. 3 C–E). These features are ~1.4 ± 0.9 μm^2 in size (Fig. 3 F), with an aspect ratio of ~1.5 ± 0.3 (Fig. 3 G). Linear regression analysis suggests that motif size varies

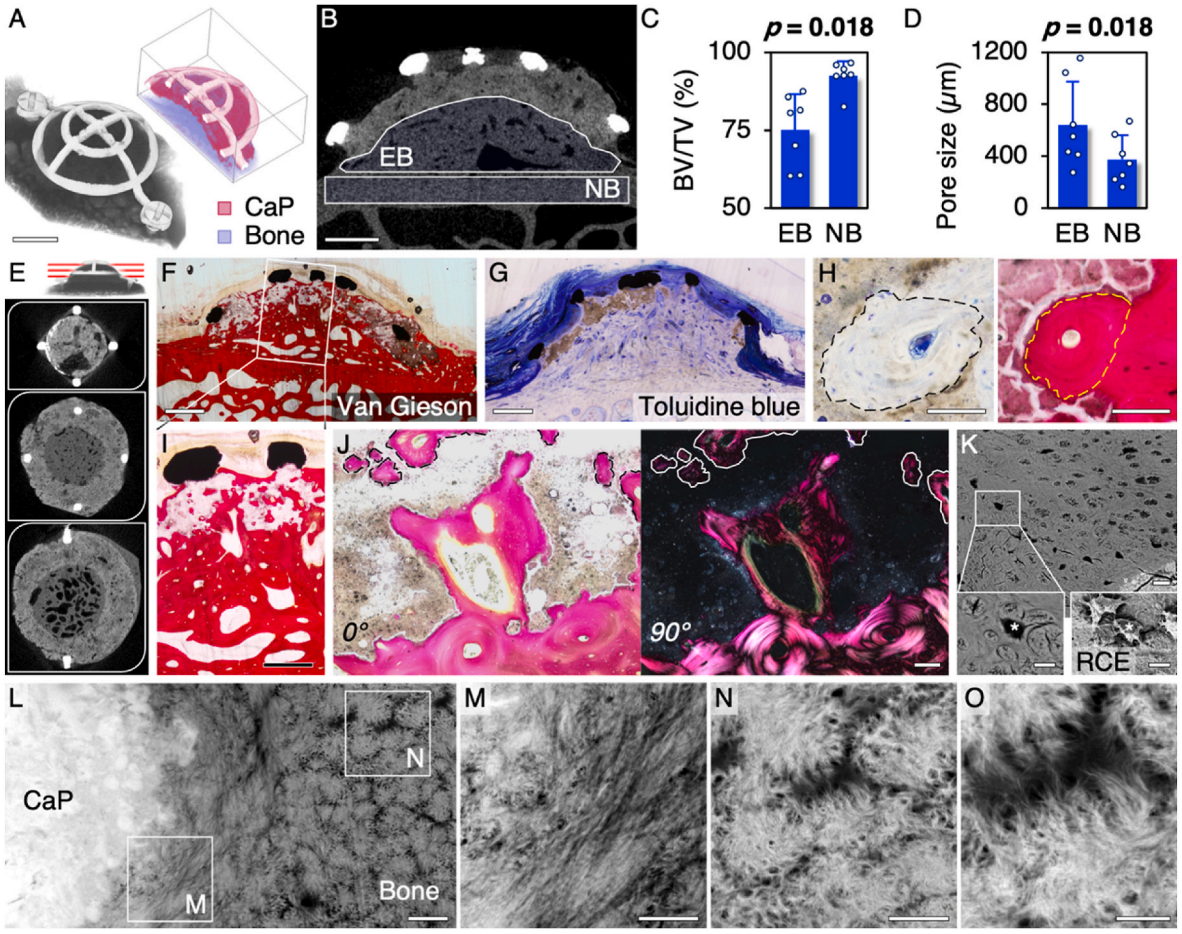

Fig. 2. Bone formation beyond the skeletal envelope. A: The dome-shaped construct. The cut view shows the Ti6Al4V frame, multi-component CaP, and bone within the dome-shaped hollow space (micro-CT). B: Regions of extraskeletal bone (EB) within the dome-shaped hollow space and native bone (NB). C: Bone volume (BV/TV) of EB and NB. D: Pore size, representing blood vessels and marrow spaces, of EB and NB. E: Axial planes at three different vertical levels within the dome-shaped hollow space. F: Histology. Van Gieson's stain. G: Histology. Toluidine blue stain. H: Remodelled osteonal bone directly abutting the CaP surface. I: Histology. Van Gieson's stain reveals bone within the CaP. J: PLM enables discriminating between highly ordered lamellar bone and disorganised woven bone. K: Evidence of endochondral-like ossification (BSE-SEM and RCE). Insets: Osteocytes (*) embedded within cartilage-like areas. RCE reveals canaliculi projecting from the osteocytes (Scale bars = 10 μm). L–O: Bone ultrastructure (HAADF-STEM). Bone-CaP interface (L). Collagen fibrils oriented parallel to the image plane. The characteristic ~67 nm periodic striations are observed (M). Rosettes (N). A highly interconnected mesh of rope-like mineralised bundles arises by virtue of collagen fibrils and associated mineral platelets that run between adjacent bundles (O). Scale bars in A, B, F, and G = 2 mm, H = 100 μm, I = 1 mm, J = 100 μm, K = 20 μm, L = 1 μm, M and N = 500 nm, and O = 200 nm. (For interpretation of the references to colour in this figure legend, the reader is referred to the Web version of this article.)

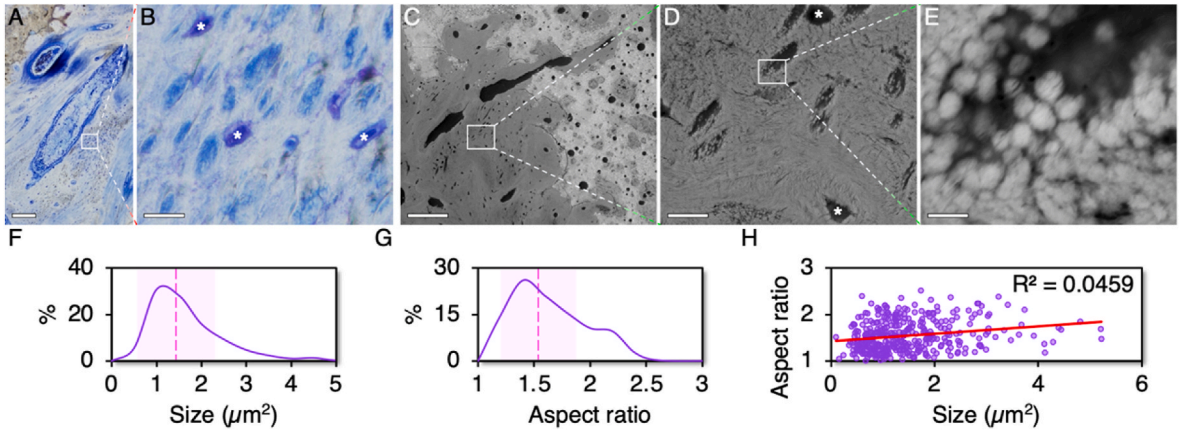

Fig. 3. Ongoing mineralisation. A–B: The process of new bone formation and subsequent mineralisation are evident directly below the CaP (* = osteocyte). C–E: Spherical to marquise-shaped motifs of mineral (* = osteocyte). F: Size distribution. Vertical line and shaded box represent the mean value ± standard deviation. G: Aspect ratio distribution. Vertical line and shaded box represent the mean value ± standard deviation. H: Relationship between size and aspect ratio (n = 377). Scale bars in A = 200 μm, B = 20 μm, C = 200 μm, D = 20 μm, and E = 2 μm.

independently of aspect ratio ($R^2 = 0.046$, $p < 0.001$), which implies the absence of preferential growth along either the axial or the radial direction, and thereby suggesting an isotropic growth pattern (Fig. 3 H). Such features have previously been identified at the bone formation front [38], and represent a key architectural building block component of bone [39].

3.4. Composition of extraskeletal bone is comparable to that of native bone

Fourier transform infrared spectroscopy [40] (Fig. 4 A) and micro-Raman spectroscopy [41] (Fig. 4 B) indicate that extracellular matrix composition of EB within the dome-shaped hollow space is comparable to that of NB. Areas where remodelling is either ongoing or has recently taken place are recognised by relatively lower mineral content (CHAp) compared to neighbouring areas of yet unremodelled woven bone observed as higher *Z*-contrast regions by BSE-SEM. Co-localisation of Amide III and CHAp signals confirms bone infiltration into the CaP bulk.

3.5. Bone inclusions within CaP bulk exhibit an expected pattern of extracellular matrix maturation

To further characterise the extracellular matrix of bone within the CaP bulk, we considered two such inclusions of *de novo* bone, one of ~100 μm diameter and the other of ~50 μm diameter, presumably representing relatively younger tissue (Fig. 5). The mineral-to-matrix ratio (MMR), carbonate-to-phosphate ratio (CO_3^{2-} content), and mineral crystallinity of these inclusions were determined using micro-Raman spectroscopy. MMR is obtained from the integral area ratio between ν_2 PO_4^{3-} and Amide III bands. CO_3^{2-} content is taken as the integral area ratio between the ν_1 CO_3^{2-} and ν_2 PO_4^{3-} bands. Mineral crystallinity is estimated as the inverse full-width at half-maximum (1/FWHM) of the ν_1 PO_4^{3-} band (940–980 cm^{-1}). The ~100 μm inclusion had an average MMR of 0.59 and CO_3^{2-} content of 0.65 (Fig. 5 A–C), while the ~50 μm inclusion had an average MMR of 0.44 and CO_3^{2-} content of 0.48 (Fig. 5 D–E). It is inferred that the increase in CO_3^{2-} content accompanies a commensurate increase in the mineral-to-matrix ratio (Fig. 5 C, E). But despite the small increase in carbonate content, the mineral crystallinity of both inclusions remains at ~0.06 (FWHM: 16.39–16.47 cm^{-1}). Interestingly, in comparison to bone apatite, the CHAp within the multi-component CaP shows broadening of the ν_1 PO_4^{3-} band (FWHM: 19.3–21.1 cm^{-1}) and therefore mineral crystallinity of ~0.05. Morphologically similar to Ca-PP observed in the intact CaP (Fig. 5 F), we identified discrete Ca-PP particles embedded within the extracellular matrix using correlative BSE-SEM and micro-Raman spectroscopy (Fig. 5 G, Fig. S11).

3.6. Osteocytes communicate with the CaP surface through the lacuno-canalicular network

Presence of osteonal bone, characterised by well-defined Haversian canals and concentric lamellae, confirms that remodelling also occurs within the CaP bulk (Fig. 6 A). RCE reveals numerous canaliculi extending between osteocytes and the CaP, both within the CaP bulk (Fig. 6 B–D) and in EB within the dome-shaped hollow space below the CaP (Fig. 6 E–G), which indicates direct biophysical interaction. Canaliculi also connect the osteocytes to each other and to the vasculature, thereby forming a comprehensive cell-cell communication network and therefore a mechanism to drive bone repair and renewal.

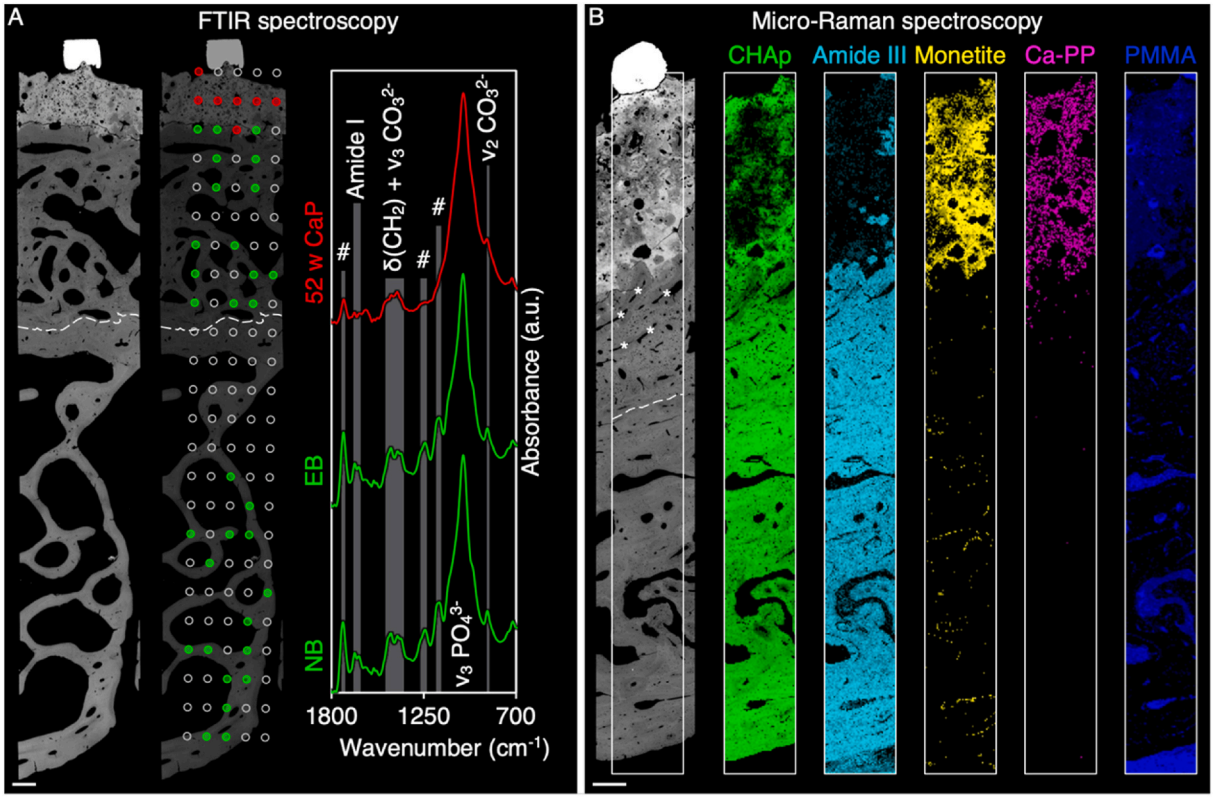

Fig. 4. Composition of extraskeletal bone and native bone. A: Fourier transform infrared (FTIR) spectroscopy. Measurement spots were included (filled circles) or excluded (empty circles) based on the quality of contact between the ATR crystal and the sample surface. # = PMMA. BSE-SEM overview. White broken line demarcates the boundary between extraskeletal bone and native bone. 52 w CaP ($n = 7$); native bone (NB; $n = 16$); extraskeletal bone (EB; $n = 15$). B: Micro-Raman spectroscopy. 1000 × 10,000 μm^2 ROI (25000 spectra). BSE-SEM overview. White broken line demarcates the boundary between native bone and extraskeletal bone. Areas of ongoing remodelling or recently remodelled sites are indicated by asterisks (*). Scale bars in A = 500 μm and B = 500 μm.

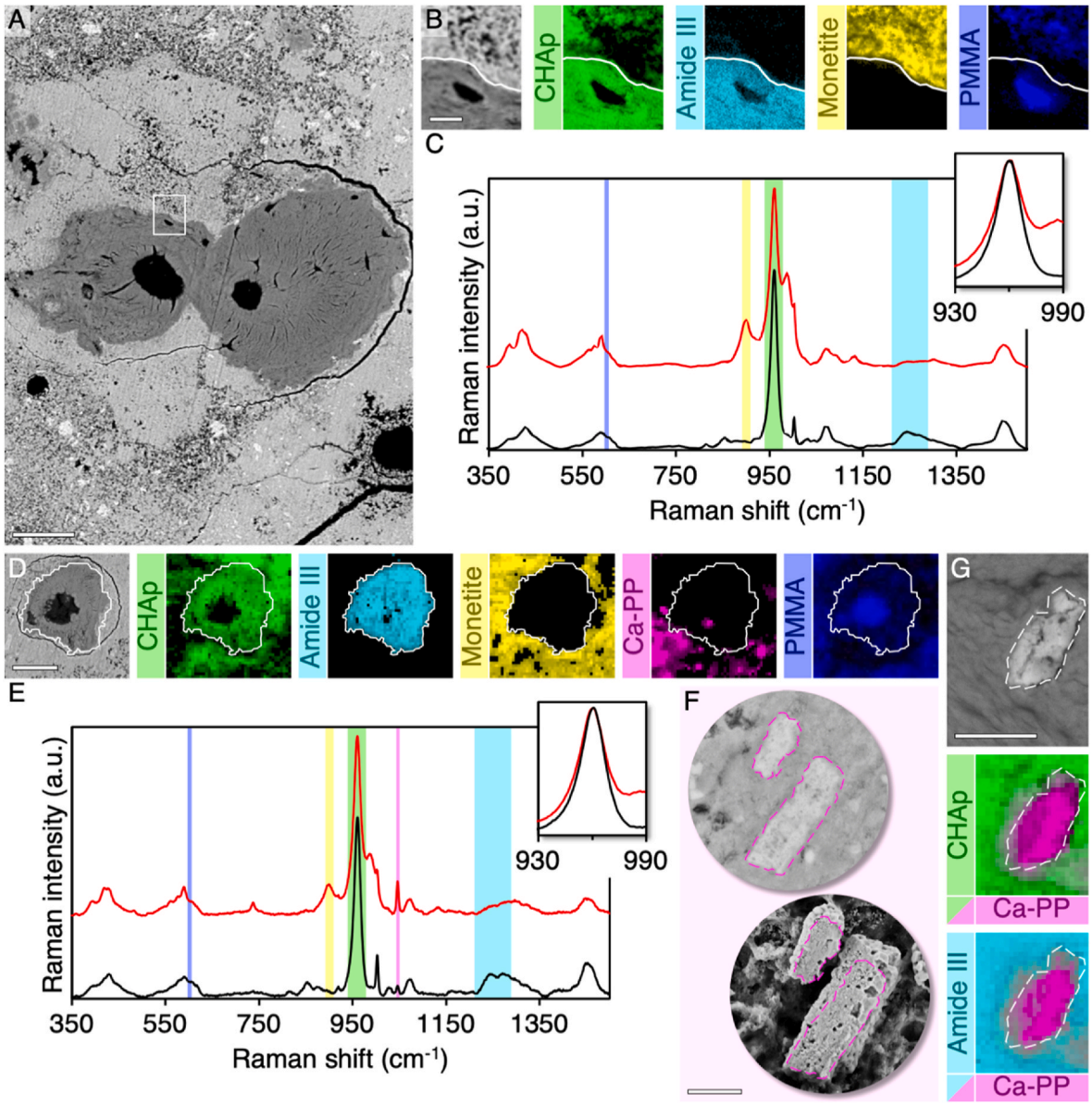

Fig. 5. Bone infiltration into the CaP bulk. A: An inclusion of *de novo* bone within the CaP, ~100 μm in diameter (BSE-SEM). B: Osteocyte adjacent to CaP (BSE-SEM and micro-Raman spectroscopy). 24 × 30 μm^2 ROI. C: Average Raman spectra of bone/collagen-containing region (3558 spectra) and non-bone/collagen-free region (4442 spectra). Inset: Detail of the 930–990 cm^{-1} region. D: An inclusion of *de novo* bone within the CaP, ~50 μm in diameter (BSE-SEM and micro-Raman spectroscopy). 90 × 90 μm^2 ROI. E: Average Raman spectra of bone/collagen-containing region (1347 spectra) and non-bone/collagen-free region (678 spectra). Inset: Detail of the 930–990 cm^{-1} region. F: Ca-PP particles in CaP bulk (BSE-SEM and RCE). G: Ca-PP particle embedded within bone extracellular matrix (BSE-SEM and micro-Raman spectroscopy). 6.3 × 6.3 μm^2 ROI. Raman maps of Ca-PP with CHAp and Amide III. Scale bars in A = 50 μm, B = 10 μm, D = 25 μm, F = 5 μm, and G = 5 μm.

To further characterise the potential capacity for mechanotransduction, we determined the osteocyte density (N.Ot/B.Ar) of NB and EB within the hollow dome-shaped space under the CaP. For this purpose, PLM enables unequivocal discrimination between woven bone (WB) areas and lamellar bone (LB) areas [42,43]. Additionally, exploiting the autoluminescence from the embedding resin, correlative brightfield and epifluorescence microscopy allows distinguishing between resin-filled osteocyte lacunae and areas of ongoing mineralisation. The latter, whilst being similar in appearance to osteocytes, stain positively for the presence of collagen with the Van Gieson's stain, hence resin-filled osteocyte lacunae are accurately identified (Fig. 6 H). Corroborating microstructural and compositional findings, N.Ot/B.Ar of EB (554 ± 66 per mm^2) is not significantly different ($p = 0.091$) from that of NB (471 ± 104 per mm^2) (Fig. 6 I). But within EB, N.Ot/B.Ar of WB (750 ± 106 per mm^2) is ~110% higher ($p = 0.018$) than LB (358 ± 45 per mm^2) (Fig. 6 J), while osteocyte lacunae in woven bone are visibly larger than those in lamellar bone. Furthermore, woven bone comprises between 25% and 55% of the total EB (Fig. 6 K).

3.7. Osteoclast cutting cones contain Ca-PP but not monetite or β-TCP

Osteoclast cutting cones, in addition to bone resorption, actively contribute to physical degradation of the CaP (Fig. 7 A–B). Based on spatial relationships, it is evident that multinucleated cells within the same cutting cone are able to remove, simultaneously, bone extracellular matrix and the CaP. BSE-SEM reveals fine particulate matter entering the cutting cones. Correlative brightfield and epifluorescence microscopy further indicate changes in density at the CaP–cutting cone

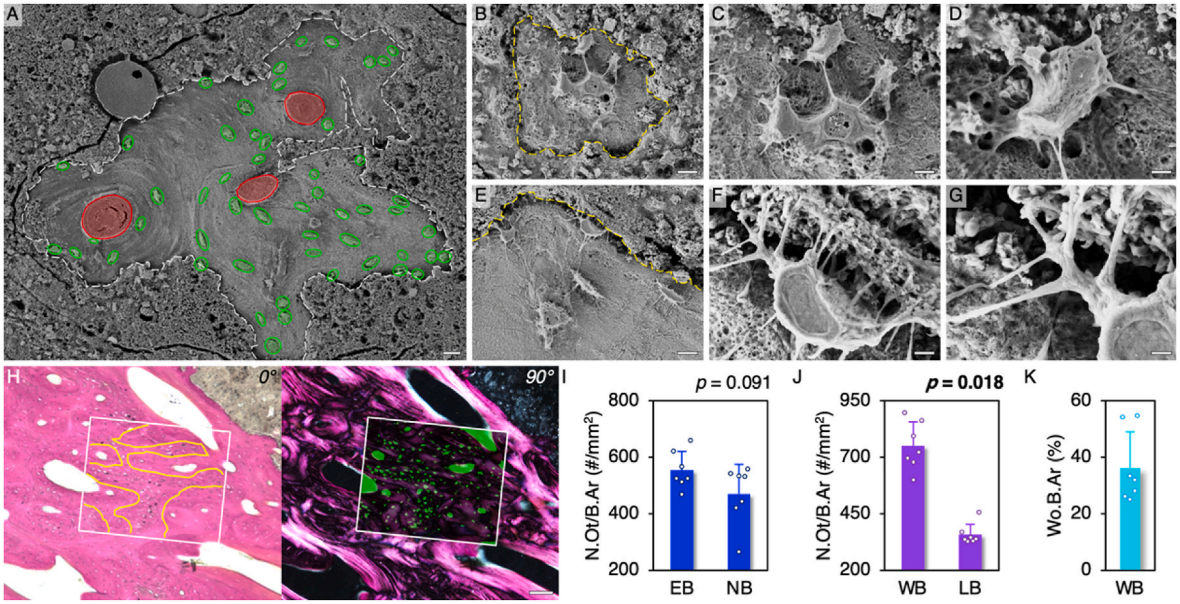

Fig. 6. Osteocyte lacuno-canalicular network as evidence of remodelling and replacement of woven bone by lamellar bone. A: Multiple Haversian canals (red) with concentrically arranged osteocytes (green) indicate remodelling within the CaP bulk (RCE). B–D: Osteocyte lacuno-canalicular network within the CaP bulk. E–G: Osteocyte lacuno-canalicular network within the dome-shaped hollow space below the CaP. H: PLM. A ROI selected for osteocyte density (N.Ot/B.Ar) quantification. Left: Yellow lines demarcate woven bone and lamellar bone areas. Right: Overlaid epifluorescence image shows regions of high and low N.Ot/B.Ar. I: Osteocyte density in extraskeletal bone (EB) and native bone (NB). Wilcoxon signed-rank test. J: Osteocyte density in woven bone (WB) and lamellar bone (LB) within extraskeletal bone. Wilcoxon signed-rank test. K: Woven bone area fraction (Wo.B.Ar) of extraskeletal bone. Scale bars in A = 20 μm, B = 10 μm, C = 5 μm, D = 2 μm, E = 10 μm, F = 2 μm, G = 1 μm, and H = 100 μm. (For interpretation of the references to colour in this figure legend, the reader is referred to the Web version of this article.)

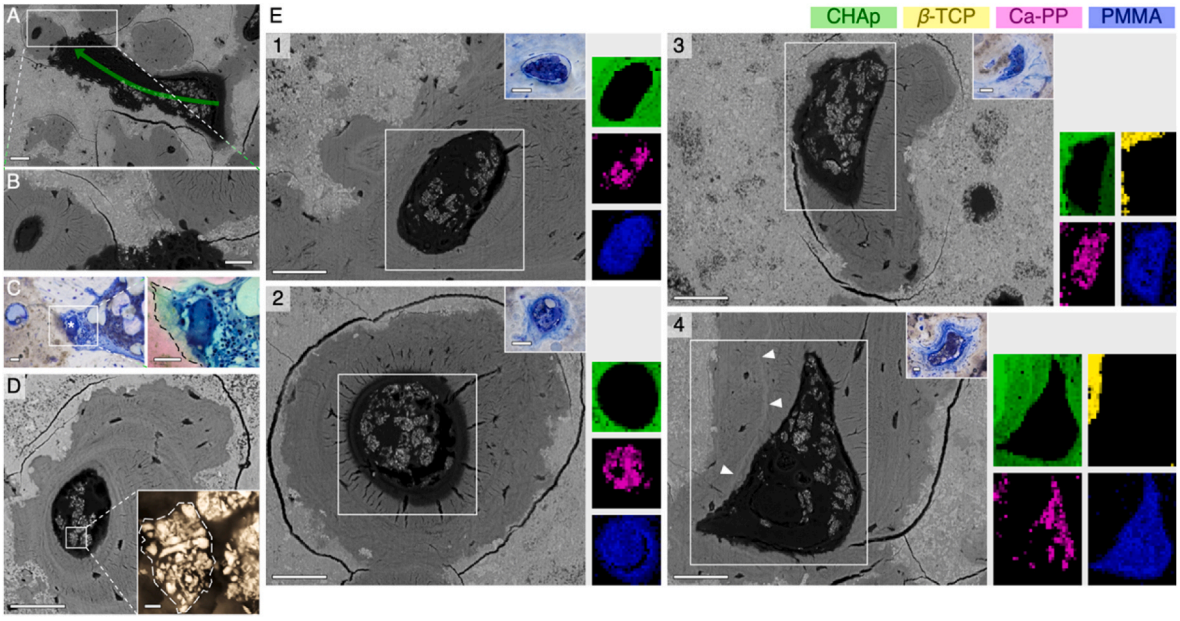

Fig. 7. Bone remodelling and CaP debris within the osteoclast cutting cone. A–B: An osteoclast cutting cone (the approximate direction of propagation is indicated) removes both the CaP and bone (BSE-SEM). C: An osteoclast in intimate contact with the CaP (*left*). Stronger autofluorescence (brightfield–epifluorescence merge) is noted at/near the CaP surface (*right*). D: CaP exists as delimited aggregations of high *Z*-contrast particulate matter within cutting cones (BSE-SEM). Inset: Detail of delimited aggregations (Scale bar = 2 μm). E: Remodelling sites caudal to the CaP (Example 1) and within the CaP bulk (Examples 2–4). CaP debris within the cutting cone is exclusively Ca-PP (BSE-SEM and micro-Raman spectroscopy). Example 1: 125 × 125 μm^2 ROI. Example 2: 125 × 125 μm^2 ROI. Example 3: 100 × 150 μm^2 ROI. Example 4: 160 × 200 μm^2 ROI. Arrowheads: Cement line. Insets in examples 1-4: Representative histological appearance of remodelling sites (Scale bars = 50 μm). Scale bars in A = 50 μm, B = 25 μm, C = 50 μm, D = 50 μm, and E = 50 μm.

interface due to localised osteoclastic activity, as interpreted from pronounced autofluorescence attributable to greater penetration of the embedding resin into the CaP (Fig. 7 C, Fig. S12). Cells within the cutting cone enclose the CaP debris as delimited aggregations that are presumably membrane-bound (Fig. 7 D), and eventually degrade the particulate matter. Regardless of the precise location with respect to the CaP (whether within the CaP bulk or in the dome-shaped hollow space), any CaP debris found within the cutting cone is exclusively Ca-PP (Fig. 7

E). It is noteworthy that, in the neighbouring CaP, even where β-TCP can still be detected and/or chemical transformation to CHAp has taken place (at least partially), the CaP debris within the cutting cone contains neither β-TCP, monetite, or CHAp. There is no indication of either additional nucleation or growth of Ca-PP crystallites. Moreover, the CaP aggregations remain fragmented and do not form dense masses.

3.8. Macrophages in soft tissues enclose Ca-PP exclusively

Staining with Lugol's solution enhances the *Z*-contrast of unmineralised tissues and enables visualisation using BSE-SEM (Fig. 8 A). Between the superficial soft tissues (i.e., skin) and the CaP, an intervening fibrous tissue layer also contains delimited aggregations of CaP debris (Fig. 8 B), enclosed within membrane-bound structures (Fig. 8 C), which are presumably macrophages (Fig. 8 D). The CaP debris contained within macrophages also comprises sub-micrometre sized particles (Fig. 8 E) that are exclusively Ca-PP, while neither β-TCP, monetite, or CHAp are detected (Fig. 8 F).

4. Discussion

The multi-component CaP formulation containing monetite, beta-tricalcium phosphate (β-TCP), and calcium pyrophosphate (Ca-PP) guides bone formation beyond the confines of the skeletal envelope, i.e., supraperiosteally. The very high bone occupancy (~75%) of the available dome-shaped hollow space and the overall composition and microstructure of extraskeletal bone (EB) similar to the native bone (NB) are testament to a favourable host response to the multi-component CaP. Notably, the mineral phase of bone in direct contact with β-TCP, monetite, and Ca-PP remains exclusively carbonated apatite [44]. The CaP itself undergoes gross physical deterioration, but large segments are unified by bone infiltration. Physical degradation, *in vivo*, is also expected to generate large quantities of readily transportable particles of the multi-component CaP. The intrinsic osteoconductive properties promote bone ingrowth into the CaP, and once the bone-CaP interface is established, the CaP surface is temporarily stabilised and protected against further degradation until an osteoclast cutting cone removes the initially formed bone together with a surrounding collar of CaP. While all of the individual constituent CaP phases are detectable after 52 weeks *in vivo,* the physiological environment encourages conversion to carbonated apatite (CHAp), though only partially. In humans, the amount of CHAp has earlier been estimated at ~6% after 31 months *in vivo* [19]. Here, we note that such spontaneously formed CHAp has lower crystallinity than bone apatite and is associated with minor Mg enrichment. Mg^{2+} ions are widely believed to inhibit apatite crystallisation and restrict crystal growth [45–47]. Moreover, in a dose-dependent manner [48], Mg^{2+} ions also behave as a stabilising impurity in β-$Ca_3(PO_4)_2$ [49]. Mg-stabilised β-$Ca_3(PO_4)_2$, erroneously also referred to as Mg-whitlockite [50], makes a frequent appearance in pathological mineralisation of various soft tissues [44], and exhibits greater chemical stability than β-$Ca_3(PO_4)_2$ [51] under physiological conditions. The absence of a characteristic Raman peak for Mg-whitlockite (at ~925 cm^{-1} [33]), however, confirms that the observed phase within the multi-component CaP after 52 weeks *in vivo* is indeed β-TCP.

When this multi-component CaP is implanted in an ovine calvarial

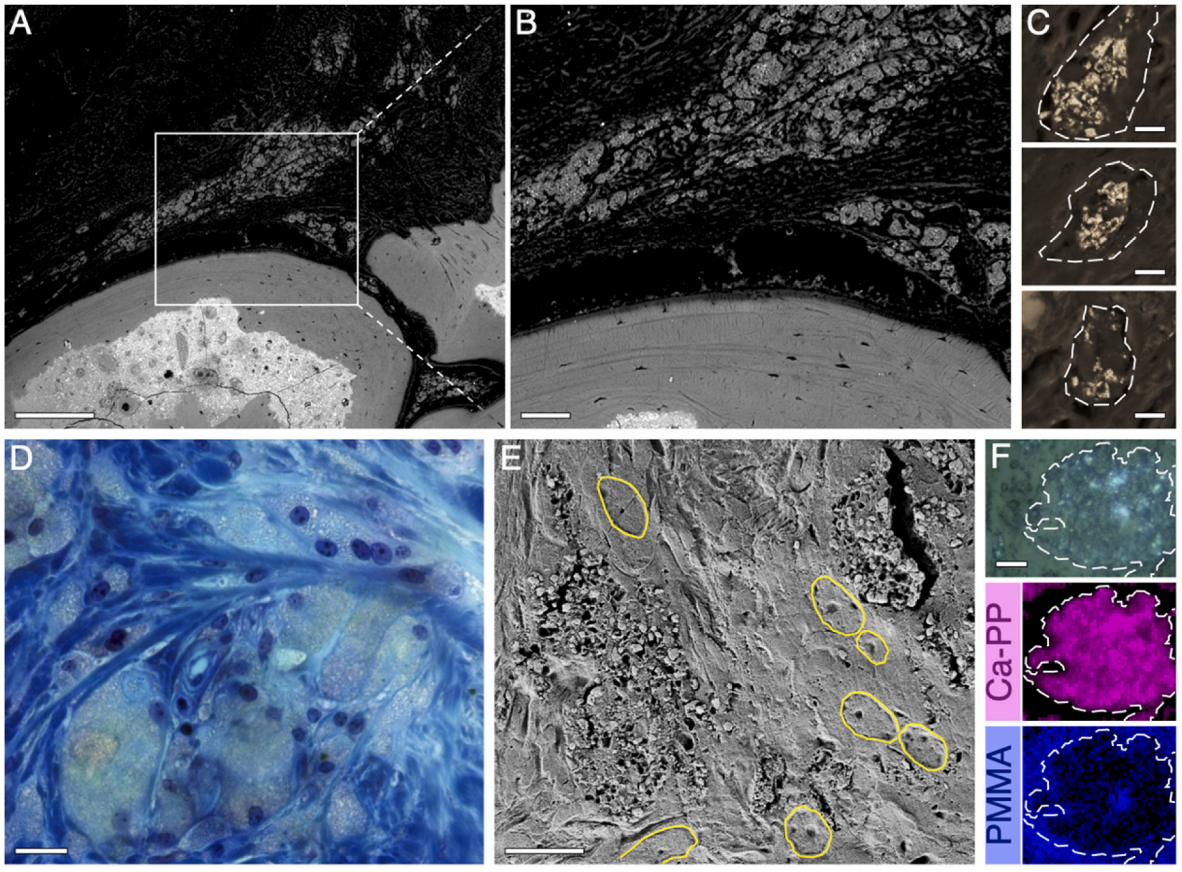

Fig. 8. CaP debris within fibrous tissue. A–B: CaP exists as delimited aggregations (BSE-SEM; I_2/KI stained). C: Delimited aggregations contain varying amounts of CaP debris (BSE-SEM; I_2/KI stained). D: Macrophages internalise CaP particles (brightfield–epifluorescence merge). E: CaP particles internalised by macrophages are sub-micrometre in size. Nuclei (yellow circles) and nucleoli are clearly visible (RCE). F: CaP within soft tissue (micro-Raman spectroscopy). 50 × 45 μm^2 ROI. Scale bars in A = 200 μm, B = 100 μm, C = 10 μm, D = 20 μm, E = 10 μm, and F = 20 μm. (For interpretation of the references to colour in this figure legend, the reader is referred to the Web version of this article.)

bone defect, the presence of mature bone of similar microstructure to the native bone, but with relatively few osteoblasts and multinucleated giant cells, suggests that an eventual state of homeostasis may be attained by 52 weeks [52]. In contrast, the present findings reveal a much more dynamic and spatio-temporally evolving picture of extraskeletal bone formed in response to a predominantly monetite-based CaP material. Bone inclusions confined to porosities within the CaP show not only a molecular signature indistinguishable from that of the native bone but also a similar maturation pattern, where higher mineral-to-matrix ratio is associated with higher CO_3^{2-} content [38]. The increase in CO_3^{2-} content is, however, insufficient to induce significant further distortion of the bone apatite lattice (i.e., mineral crystallinity) [53] or is compensated for by a progressive increase in crystallite size. At sites of ongoing mineralisation, we detected marquise-shaped motifs, whose dimensions are in close agreement with CaP-containing matrix vesicles in the extracellular space around osteoblasts, *in vitro* [54], and isolated from the mineralisation front, *in vivo* [55], strongly pointing towards a normal and expected pathway of bone biomineralisation.

Osteoclast cutting cones play a key but passive role in the creation of irregularly shaped CaP islands, apparently discontinuous from the CaP bulk, embedded '*between*' different packets of bone rather than '*within*' an individual packet of bone. Mechanistically, following initial bone infiltration into the CaP bulk, osteoclast cutting cones propagating in mutually disparate directions, in the process of resorbing previously formed bone also remove some of the surrounding CaP. Qualitatively, the individual packets of bone abutting these CaP islands vary in tissue age, as judged from their microstructure and the degree of mineralisation, indicating that multiple cutting cones do not actively, and/or simultaneously, converge upon a specific target area of the CaP. This further suggests that these CaP islands have not passively broken away from the CaP bulk and subsequently become entrapped in the forming bone.

In a leporine segmental radius defect model, a recent investigation of a similar multi-component CaP composition reports the presence of CaP particles within multinucleated cells after 12 weeks [56]. However, their precise phase composition was not investigated. The present data indicate that the CaP particles within multinucleated cells, whether at osseous sites (i.e., osteoclasts within cutting cones) or at non-osseous sites (i.e., macrophages within fibrous tissue), are exclusively Ca-PP. While an inhibitory action of pyrophosphate ions on osteoclasts has recently been proposed [57], it is evident that the local (i.e., intracellular) environment of multinucleated cells is neither supportive of apatite precipitation nor favourable to the chemical stability of monetite or β-TCP. Indeed, the solubilities of β-TCP and monetite are one and two orders of magnitude, respectively, higher than HAp [58]. CHAp, too, exhibits higher solubility than nominally carbonate-free apatites [59–61]. In comparison, Ca-PP is minimally soluble in aqueous media, but although acidic pH and presence of Mg^{2+} ions can slightly raise the solubility [62], any biological environment is considered replete with Ca^{2+} and PO_4^{3-} ions, which further contribute to decreased solubility [63].

Osteocytes are the mechanotransducers in bone [64]. The finding of well-established osteocyte lacuno-canalicular networks in extraskeletal bone and bone inclusions within the CaP indicates that bone possesses the necessary infrastructure to detect and respond to mechanical loading. The osteocyte lacuno-canalicular network plays a critical role in bone maintenance around non-degradable biomaterials [65]. More recently it has been suggested that the lacuno-canalicular system facilitates the transport of mineral ions [66]. Therefore, direct physical communication between the CaP surface and canaliculi suggests the possibility for transport of Ca^{2+} and PO_4^{3-} ions between a reservoir (i.e., the multi-component CaP) and rapidly forming bone where the need for Ca^{2+} and PO_4^{3-} may be particularly high.

The overall pattern of bone formation within the hollow space is consistent with established principles of fracture healing, where both intramembranous and endochondral ossification are observed [67]. It is noteworthy that in the current scenario, although no osteotomy had been performed, haematoma formation within the hollow space presumably acts as the main driving force behind osteogenesis at this extraskeletal site. Histological observations indicate that woven bone forms as the first step, and is gradually remodelled and replaced by lamellar/osteonal bone. A significant amount of woven bone is still present at 52 weeks, particularly in the vicinity of the CaP, and is being replaced by lamellar bone, which attests in favour of the observation that extraskeletal bone is built up in a recurring manner. Here, bone apposition on the surface of previously formed bone together with condensation of mesenchymal osteoprogenitor cells into foci of woven bone and, to a lesser extent, bone formation via a cartilage-like precursor contribute significantly to the total osteogenesis. These processes followed by remodelling and vascularisation indicate that this extraskeletal bone is vital and capable of self-renewal. It is well-understood that hypertrophic chondrocytes, under appropriate conditions, can dedifferentiate–redifferentiate or directly transdifferentiate to osteoblast-like cells and contribute to osteogenesis [68,69]. In the presence of ascorbic acid, *in vitro*, hypertrophic chondrocytes switch over from producing types II and X collagens (cartilage-characteristic) to type I collagen (bone-characteristic) and assemble a mineralising extracellular matrix [70]. Moreover, during endochondral ossification, hypertrophic chondrocytes are coupled to the recruitment of osteoblasts, osteoclasts, and blood cells [71], and release vascular endothelial growth factor (VEGF), which is an essential coordinator of chondrocyte apoptosis, chondroclast function, extracellular matrix remodelling, angiogenesis, and bone formation in the growth plate [72].

Currently, the long-term fate of extraskeletal bone, i.e., much after the multi-component CaP is completely eliminated, remains poorly understood. Compared to the native bone, pores in extraskeletal bone are, on average, ~70% larger. The largest of these pores contain bone marrow – a characteristic feature of trabecular bone. But despite being a source of several important cell types, development of marrow cavities reveals a potentially undesirable scenario. A mixed cortical–trabecular architecture of extraskeletal bone hints at intracortical remodelling and the start of trabecularisation (of the cortex) [73]. Given the lack of information on the molecular mechanisms underlying this particular case of intracortical remodelling, we speculate along the lines of disuse osteoporosis [74]. But if such loss of bone mass is indeed due to skeletal unloading, it is prudent to ask whether all of the extraskeletal bone will eventually undergo resorption after cessation of pro-osteogenic stimulation from the CaP. From a clinical perspective, there is an urgent need to promote both horizontal and vertical bone regeneration in edentulous patients, employing so-called guided bone regeneration using resorbable and non-resorbable membranes, respectively [16]. Insertion of intraoral implants at sites augmented by extraskeletal bone in hollow CaP domes will most likely alter the peri-implant bone architecture according to loading directions and the timing of implant insertion, eventually leading to corticalisation. Therefore, the translational opportunities leading to clinical use of the present experimental observations are evident.

Formation of extraskeletal bone, here, is not in perfect agreement with the currently accepted description of heterotopic bone induction in response to biomaterials, which requires *in vivo* testing at anatomical sites (i.e., soft tissues) "*where bone does not naturally grow*" [75]. More recently, intrinsic osteoinduction has been attributed to the ability of a material to bring about local depletion (rather than accumulation) of Ca^{2+} and PO_4^{3-} ions as a result of precipitation of a *bioactive* CHAp, for example if consumption exceeds the supply of these ions [76]. Although CHAp precipitation does occur (and the Ca/P ratio of the multi-component CaP increases) *in vivo*, whether there is a local reduction in the concentrations of Ca^{2+} and PO_4^{3-} ions remains challenging to ascertain.

The absence of an early healing endpoint (e.g., 3–6 months) and cellular/molecular analyses (e.g., immunohistochemistry and gene

expression analysis) are identified as potential limitations. Therefore, the precise sequence of biological events underpinning bone formation outside the physiological boundary remains elusive. Of further importance is to determine the exact phenotypes and molecular activities of the various cells involved not only in bone formation but also in biomaterial degradation and replacement by remodelled bone. For this purpose, future investigations should employ techniques permissive of site-specific molecular analysis, e.g., laser-capture microdissection and gene expression analysis, in order to reveal the role(s) of the different cell types with respect to their spatial distribution around this multi-component CaP.

In summary, this work demonstrates that bone formation beyond the physiological skeletal envelope, achieved with a multi-component CaP comprising monetite, β-TCP, and Ca-PP, follows the same biological patterns as the development of native bone and fracture healing, including endochondral ossification. In addition to remodelling and replacement of rapidly forming woven bone, extensive vascularisation enables a constant availability of osteoprogenitor cells and inflammatory cells, and a comprehensive mechanism for nutrient transport. Furthermore, an extensive osteocyte lacuno-canalicular network provides the necessary infrastructure for mechanotransduction, self-repair, and renewal. These findings open up a wide range of avenues for guided bone regeneration, particularly of large bone defects that cannot heal spontaneously. Additionally, ions such as Mg^{2+}, Si^{4+}, Mn^{2+}, Zn^{2+}, and Sr^{2+} can be introduced into CaPs for their possible biological relevance [77]. It is also evident that large volumes of bone can be formed via a synthetic, porous CaP formulation that osteoclasts are able to remove and is sequestered by multinucleated cells in unmineralised tissues, without the need to introduce either stem cells or growth factors and cytokines into a tissue engineering scaffold.

Data and materials availability

All data are available in the main text or the supplementary materials.

CRediT authorship contribution statement

Furqan A. Shah: Conceptualization, Methodology, Investigation, Visualization, Supervision, Writing – original draft, Writing – review & editing, Funding acquisition. **Martina Jolic:** Methodology, Investigation, Visualization, Writing – original draft, Writing – review & editing. **Chiara Micheletti:** Methodology, Investigation, Visualization, Writing – original draft. **Omar Omar:** Conceptualization, Animal surgery, Writing – review & editing. **Birgitta Norlindh:** Sample preparation. **Lena Emanuelsson:** Sample preparation. **Håkan Engqvist:** Conceptualization, Funding acquisition. **Thomas Engstrand:** Conceptualization. **Anders Palmquist:** Methodology, Investigation, Writing – original draft, Funding acquisition. **Peter Thomsen:** Conceptualization, Supervision, Writing – original draft, Writing – review & editing, Funding acquisition.

Declaration of competing interest

PT is a shareholder of OssDsign AB. TE and HE serve as consultants with OssDsign AB, are shareholders of OssDsign AB, and have two patents (US20130066324A130 and US9220597B232) relevant to this work.

Acknowledgments

The authors wish to thank Mats Hulander (PhD) and Katarina Logg (PhD) at Chalmers University of Technology for access to PLM and FTIR facilities. Financial support was received from the BIOMATCELL VINN Excellence Center of Biomaterials and Cell Therapy, the Västra Götaland Region, the Swedish Research Council (2017-04728, 2018-02891, and 2020-04715), the Swedish Foundation for Strategic Research (RMA15-0110), the Swedish state under the agreement between the Swedish government and the county councils, the ALF agreement (ALFGBG-725641), the IngaBritt and Arne Lundberg Foundation, the Hjalmar Svensson Foundation, the Adlerbertska Foundation, the Kungliga Vetenskaps- och Vitterhets-Samhället i Göteborg, the Eivind och Elsa K: son Sylvans Stiftelse, and the Area of Advance Materials of Chalmers and GU Biomaterials within the Strategic Research Area initiative launched by the Swedish government. The funding sources had no role in the conceptualisation, design, data collection, analysis, decision to publish, or preparation of the manuscript. All listed funding sources provided research grants that covered materials, consumables, equipment, and the salaries of the University of Gothenburg (OO, FAS, AP, and PT) and Uppsala University (HE) employees.

Appendix A. Supplementary data

Supplementary data to this article can be found online at https://doi.org/10.1016/j.bioactmat.2022.03.012.

References

[1] F. Shapiro, Bone development and its relation to fracture repair. The role of mesenchymal osteoblasts and surface osteoblasts, Eur. Cell. Mater. 15 (2008) 53–76.
[2] C. Ferguson, E. Alpern, T. Miclau, J.A. Helms, Does adult fracture repair recapitulate embryonic skeletal formation? Mech. Dev. 87 (1–2) (1999) 57–66.
[3] R. Marsell, T.A. Einhorn, The biology of fracture healing, Injury 42 (6) (2011) 551–555.
[4] A. Vetter, D.R. Epari, R. Seidel, H. Schell, P. Fratzl, G.N. Duda, R. Weinkamer, Temporal tissue patterns in bone healing of sheep, J. Orthop. Res. 28 (11) (2010) 1440–1447.
[5] D. Lacroix, P.J. Prendergast, A mechano-regulation model for tissue differentiation during fracture healing: analysis of gap size and loading, J. Biomech. 35 (9) (2002) 1163–1171.
[6] T.A. Einhorn, L.C. Gerstenfeld, Fracture healing: mechanisms and interventions, Nat. Rev. Rheumatol. 11 (1) (2015) 45–54.
[7] D.J. Hadjidakis, Androulakis, II, bone remodeling, Ann. N. Y. Acad. Sci. 1092 (2006) 385–396.
[8] R. Dimitriou, E. Jones, D. McGonagle, P.V. Giannoudis, Bone regeneration: current concepts and future directions, BMC Med. 9 (1) (2011) 66.
[9] T.W. Bauer, G.F. Muschler, Bone graft materials. An overview of the basic science, Clin. Orthop. Relat. Res. 371 (2000) 10–27.
[10] C.G. Finkemeier, Bone-grafting and bone-graft substitutes, J. Bone Joint Surg. Am. 84 (3) (2002) 454–464.
[11] K.A. Hing, Bone repair in the twenty–first century: biology, chemistry or engineering? Philos. Trans. R. Soc. London, Ser. A: Math., Phys. Eng. Sci. 362 (1825) (2004) 2821–2850.
[12] W. Habraken, P. Habibovic, M. Epple, M. Bohner, Calcium phosphates in biomedical applications: materials for the future? Mater. Today 19 (2) (2016) 69–87.
[13] R.Z. LeGeros, Calcium phosphate-based osteoinductive materials, Chem. Rev. 108 (11) (2008) 4742–4753.
[14] P. Habibovic, H. Yuan, C.M. van der Valk, G. Meijer, C.A. van Blitterswijk, K. de Groot, 3D microenvironment as essential element for osteoinduction by biomaterials, Biomaterials 26 (17) (2005) 3565–3575.
[15] M. Retzepi, N. Donos, Guided Bone Regeneration: biological principle and therapeutic applications, Clin. Oral Implants Res. 21 (6) (2010) 567–576.
[16] I. Elgali, O. Omar, C. Dahlin, P. Thomsen, Guided bone regeneration: materials and biological mechanisms revisited, Eur. J. Oral Sci. 125 (5) (2017) 315–337.
[17] J. Anderud, R. Jimbo, P. Abrahamsson, E. Adolfsson, J. Malmström, A. Wennerberg, The impact of surface roughness and permeability in hydroxyapatite bone regeneration membranes, Clin. Oral Implants Res. 27 (8) (2016) 1047–1054.
[18] O. Omar, T. Engstrand, L. Kihlström Burenstam Linder, J. Åberg, F.A. Shah, A. Palmquist, U. Birgersson, I. Elgali, M. Pujari-Palmer, H. Engqvist, P. Thomsen, In Situ Bone Regeneration of Large Cranial Defects Using Synthetic Ceramic Implants with a Tailored Composition and Design, Proc Natl Acad Sci U S A, 2020, p. 202007635.
[19] S. Lewin, L. Kihlström Burenstam Linder, U. Birgersson, S. Gallinetti, J. Åberg, H. Engqvist, C. Persson, C. Öhman-Mägi, Monetite-based composite cranial implants demonstrate long-term clinical volumetric balance by concomitant bone formation and degradation, Acta Biomater. 128 (2021) 502–513.
[20] H. Zhou, L. Yang, U. Gbureck, S.B. Bhaduri, P. Sikder, Monetite, an important calcium phosphate compound–Its synthesis, properties and applications in orthopedics, Acta Biomater. 127 (2021) 41–55.
[21] F. Tamimi, Z. Sheikh, J. Barralet, Dicalcium phosphate cements: brushite and monetite, Acta Biomater. 8 (2) (2012) 474–487.
[22] M. Bohner, G. Baroud, A. Bernstein, N. Döbelin, L. Galea, B. Hesse, R. Heuberger, S. Meille, P. Michel, B. von Rechenberg, J. Sague, H. Seeherman, Characterization

and distribution of mechanically competent mineralized tissue in micropores of β-tricalcium phosphate bone substitutes, Mater. Today 20 (3) (2017) 106–115.
[23] H. Fleisch, S. Bisaz, Mechanism of calcification: inhibitory role of pyrophosphate, Nature 195 (1962) 911.
[24] C. Thouverey, G. Bechkoff, S. Pikula, R. Buchet, Inorganic pyrophosphate as a regulator of hydroxyapatite or calcium pyrophosphate dihydrate mineral deposition by matrix vesicles, Osteoarthritis Cartilage 17 (1) (2009) 64–72.
[25] W.N. Addison, F. Azari, E.S. Sørensen, M.T. Kaartinen, M.D. McKee, Pyrophosphate inhibits mineralization of osteoblast cultures by binding to mineral, up-regulating osteopontin, and inhibiting alkaline phosphatase activity, J. Biol. Chem. 282 (21) (2007) 15872–15883.
[26] L. Bouchard, R. de Médicis, A. Lussier, P.H. Naccache, P.E. Poubelle, Inflammatory microcrystals alter the functional phenotype of human osteoblast-like cells in vitro: synergism with IL-1 to overexpress cyclooxygenase-2, J. Immunol. (Baltimore, Md.) 168 (10) (2002) 5310–5317, 1950.
[27] Y. Xu, T.F. Cruz, K.P. Pritzker, Alkaline phosphatase dissolves calcium pyrophosphate dihydrate crystals, J. Rheumatol. 18 (10) (1991) 1606–1610.
[28] T. Shinozaki, K.P. Pritzker, Regulation of alkaline phosphatase: implications for calcium pyrophosphate dihydrate crystal dissolution and other alkaline phosphatase functions, J. Rheumatol. 23 (4) (1996) 677–683.
[29] F.H. Lin, C.C. Lin, C.M. Lu, H.C. Liu, J.S. Sun, C.Y. Wang, Mechanical properties and histological evaluation of sintered beta-Ca2P2O7 with Na4P2O7.10H2O addition, Biomaterials 16 (10) (1995) 793–802.
[30] L.M. Grover, A.J. Wright, U. Gbureck, A. Bolarinwa, J. Song, Y. Liu, D.F. Farrar, G. Howling, J. Rose, J.E. Barralet, The effect of amorphous pyrophosphate on calcium phosphate cement resorption and bone generation, Biomaterials 34 (28) (2013) 6631–6637.
[31] F.A. Shah, K. Ruscsák, A. Palmquist, Mapping bone surface composition using real-time surface tracked micro-Raman spectroscopy, Cells Tissues Organs 209 (4–6) (2020) 266–275.
[32] F.A. Shah, Characterization of synthetic hydroxyapatite fibers using high-resolution, polarized Raman spectroscopy, Appl. Spectrosc. (2020), 3702820942540.
[33] B. Wopenka, J.D. Pasteris, A mineralogical perspective on the apatite in bone, Mater. Sci. Eng .C Mater. Biol. Appl. 25 (2) (2005) 131–143.
[34] C. Baccin, J. Al-Sabah, L. Velten, P.M. Helbling, F. Grünschläger, P. Hernández-Malmierca, C. Nombela-Arrieta, L.M. Steinmetz, A. Trumpp, S. Haas, Combined single-cell and spatial transcriptomics reveal the molecular, cellular and spatial bone marrow niche organization, Nat. Cell Biol. 22 (1) (2020) 38–48.
[35] A. Boyde, Staining plastic blocks with triiodide to image cells and soft tissues in backscattered electron SEM of skeletal and dental tissues, Eur. Cell. Mater. 24 (2012) 154–161.
[36] K. Grandfield, V. Vuong, H.P. Schwarcz, Ultrastructure of bone: hierarchical features from nanometer to micrometer scale revealed in focused ion beam sections in the TEM, Calcif. Tissue Int. (2018).
[37] Y. Liu, I. Manjubala, H. Schell, D.R. Epari, P. Roschger, G.N. Duda, P. Fratzl, Size and habit of mineral particles in bone and mineralized callus during bone healing in sheep, J. Bone Miner. Res. 25 (9) (2010) 2029–2038.
[38] F.A. Shah, K. Ruscsák, A. Palmquist, Transformation of bone mineral morphology: from discrete marquise-shaped motifs to a continuous interwoven mesh, Bone Rep. (2020), 100283.
[39] D.M. Binkley, J. Deering, H. Yuan, A. Gourrier, K. Grandfield, Ellipsoidal mesoscale mineralization pattern in human cortical bone revealed in 3D by plasma focused ion beam serial sectioning, J. Struct. Biol. 212 (2) (2020) 107615.
[40] L. Imbert, S. Gourion-Arsiquaud, E. Villarreal-Ramirez, L. Spevak, H. Taleb, M.C. H. van der Meulen, R. Mendelsohn, A.L. Boskey, Dynamic structure and composition of bone investigated by nanoscale infrared spectroscopy, PLoS One 13 (9) (2018), e0202833.
[41] G.S. Mandair, M.D. Morris, Contributions of Raman spectroscopy to the understanding of bone strength, BoneKEy Rep 4 (2015).
[42] F. Shapiro, K. Maguire, S. Swami, H. Zhu, E. Flynn, J. Wang, J.Y. Wu, Histopathology of osteogenesis imperfecta bone. Supramolecular assessment of cells and matrices in the context of woven and lamellar bone formation using light, polarization and ultrastructural microscopy, Bone Rep. 14 (2021) 100734.
[43] F. Shapiro, J.Y. Wu, Woven bone overview: structural classification based on its integral role in developmental, repair and pathological bone formation throughout vertebrate groups, Eur. Cell. Mater. 38 (2019) 137–167.
[44] F.A. Shah, Magnesium whitlockite – omnipresent in pathological mineralisation of soft tissues but not a significant inorganic constituent of bone, Acta Biomater 125 (2021) 72–82.
[45] A. Bigi, G. Falini, E. Foresti, A. Ripamonti, M. Gazzano, N. Roveri, Magnesium influence on hydroxyapatite crystallization, J. Inorg. Biochem. 49 (1) (1993) 69–78.
[46] H. Ding, H. Pan, X. Xu, R. Tang, Toward a detailed understanding of magnesium ions on hydroxyapatite crystallization inhibition, Cryst. Growth Des. 14 (2) (2014) 763–769.
[47] A.D. Ter Braake, P.T. Tinnemans, C.M. Shanahan, J.G.J. Hoenderop, J.H.F. de Baaij, Magnesium prevents vascular calcification in vitro by inhibition of hydroxyapatite crystal formation, Sci. Rep. 8 (1) (2018) 2069.
[48] X. Li, A. Ito, Y. Sogo, X. Wang, R.Z. LeGeros, Solubility of Mg-containing beta-tricalcium phosphate at 25 degrees C, Acta Biomater 5 (1) (2009) 508–517.
[49] L.W. Schroeder, B. Dickens, W.E. Brown, Crystallographic studies of the role of Mg as a stabilizing impurity in β-Ca3(PO4)2. II. Refinement of Mg-containing β-Ca3 (PO4)2, J. Solid State Chem. 22 (3) (1977) 253–262.
[50] B. Dickens, L.W. Schroeder, W.E. Brown, Crystallographic studies of the role of Mg as a stabilizing impurity in β-Ca3(PO4)2. The crystal structure of pure β-Ca3(PO4) 2, J. Solid State Chem. 10 (3) (1974) 232–248.
[51] F.C. Driessens, Physiology of hard tissues in comparison with the solubility of synthetic calcium phosphates, Ann. N. Y. Acad. Sci. 523 (1988) 131–136.
[52] S. Gallinetti, L.K. Burenstam Linder, J. Åberg, C. Illies, H. Engqvist, U. Birgersson, Titanium reinforced calcium phosphate improves bone formation and osteointegration in ovine calvaria defects: a comparative 52-weeks study, Biomed. Mater. (2020).
[53] F.A. Shah, Towards refining Raman spectroscopy-based assessment of bone composition, Sci. Rep. 10 (1) (2020) 16662.
[54] S. Boonrungsiman, E. Gentleman, R. Carzaniga, N.D. Evans, D.W. McComb, A. E. Porter, M.M. Stevens, The role of intracellular calcium phosphate in osteoblast-mediated bone apatite formation, Proc. Natl. Acad. Sci. U. S. A. 109 (35) (2012) 14170–14175.
[55] R.J. Midura, A. Vasanji, X. Su, A. Wang, S.B. Midura, J.P. Gorski, Calcospherulites isolated from the mineralization front of bone induce the mineralization of type I collagen, Bone 41 (6) (2007) 1005–1016.
[56] T. Mellgren, A. Trbakovic, A. Thor, S. Ekman, C. Ley, C. Öhman-Mägi, P. H. Johansson, M. Jensen-Waern, P. Hedenqvist, Guided bone tissue regeneration using a hollow calcium phosphate based implant in a critical size rabbit radius defect, Biomed. Mater. (2021).
[57] B. Le Gars Santoni, L. Niggli, S. Dolder, O. Loeffel, G.A. Sblendorio, R. Heuberger, Y. Maazouz, C. Stähli, N. Döbelin, P. Bowen, W. Hofstetter, M. Bohner, Effect of minor amounts of β-calcium pyrophosphate and hydroxyapatite on the physico-chemical properties and osteoclastic resorption of β-tricalcium phosphate cylinders, Bioact. Mater. (2021).
[58] S.V. Dorozhkin, Bioceramics of calcium orthophosphates, Biomaterials 31 (7) (2010) 1465–1485.
[59] M. Okazaki, Y. Moriwaki, T. Aoba, Y. Doi, J. Takahashi, H. Kimura, Crystallinity changes of CO3-apatites in solutions at physiological pH, Caries Res 16 (4) (1982) 308–314.
[60] R.Z. LeGeros, M.S. Tung, Chemical stability of carbonate- and fluoride-containing apatites, Caries Res 17 (5) (1983) 419–429.
[61] R.Z. LeGeros, R. Kijkowska, C. Bautista, J.P. LeGeros, Synergistic effects of magnesium and carbonate on properties of biological and synthetic apatites, Connect. Tissue Res. 33 (1–3) (1995) 203–209.
[62] R.M. Bennett, J.R. Lehr, D.J. McCarty, Factors affecting the solubility of calcium pyrophosphate dihydrate crystals, JCI (J. Clin. Investig.) 56 (6) (1975) 1571–1579.
[63] D.J. McCarty, S.D. Solomon, M.L. Warnock, E. Paloyan, Inorganic pyrophosphate concentrations in the synovial fluid of arthritic patients, J. Lab. Clin. Med. 78 (2) (1971) 216–229.
[64] L. Qin, W. Liu, H. Cao, G. Xiao, Molecular mechanosensors in osteocytes, Bone Res. 8 (1) (2020) 23.
[65] F.A. Shah, P. Thomsen, A. Palmquist, A review of the impact of implant biomaterials on osteocytes, J. Dent. Res. 97 (9) (2018) 977–986.
[66] Z. Zou, T. Tang, E. Macías-Sánchez, S. Sviben, W.J. Landis, L. Bertinetti, P. Fratzl, Three-dimensional structural interrelations between cells, extracellular matrix, and mineral in normally mineralizing avian leg tendon, Proc. Natl. Acad. Sci. (2020), 201917932.
[67] H. Isaksson, W. Wilson, C.C. van Donkelaar, R. Huiskes, K. Ito, Comparison of biophysical stimuli for mechano-regulation of tissue differentiation during fracture healing, J. Biomech. 39 (8) (2006) 1507–1516.
[68] D.P. Hu, F. Ferro, F. Yang, A.J. Taylor, W. Chang, T. Miclau, R.S. Marcucio, C. S. Bahney, Cartilage to bone transformation during fracture healing is coordinated by the invading vasculature and induction of the core pluripotency genes, Development (Camb.) 144 (2) (2017) 221–234.
[69] P. Aghajanian, S. Mohan, The art of building bone: emerging role of chondrocyte-to-osteoblast transdifferentiation in endochondral ossification, Bone Res. 6 (1) (2018) 19.
[70] P. Bianco, F.D. Cancedda, M. Riminucci, R. Cancedda, Bone formation via cartilage models: the "borderline" chondrocyte, Matrix Biol 17 (3) (1998) 185–192.
[71] L.C. Gerstenfeld, F.D. Shapiro, Expression of bone-specific genes by hypertrophic chondrocytes: implication of the complex functions of the hypertrophic chondrocyte during endochondral bone development, J. Cell. Biochem. 62 (1) (1996) 1–9.
[72] H.P. Gerber, T.H. Vu, A.M. Ryan, J. Kowalski, Z. Werb, N. Ferrara, VEGF couples hypertrophic cartilage remodeling, ossification and angiogenesis during endochondral bone formation, Nat. Med. 5 (6) (1999) 623–628.
[73] R.M. Zebaze, A. Ghasem-Zadeh, A. Bohte, S. Iuliano-Burns, M. Mirams, R.I. Price, E.J. Mackie, E. Seeman, Intracortical remodelling and porosity in the distal radius and post-mortem femurs of women: a cross-sectional study, Lancet 375 (9727) (2010) 1729–1736.
[74] T. Rolvien, M. Amling, Disuse Osteoporosis: Clinical and Mechanistic Insights, Calcified Tissue International, 2021.
[75] A.M. Barradas, H. Yuan, C.A. van Blitterswijk, P. Habibovic, Osteoinductive biomaterials: current knowledge of properties, experimental models and biological mechanisms, Eur. Cell. Mater. 21 (2011) 407–429. ; discussion 429.
[76] M. Bohner, R.J. Miron, A proposed mechanism for material-induced heterotopic ossification, Mater. Today 22 (2019) 132–141.
[77] E. Boanini, M. Gazzano, A. Bigi, Ionic substitutions in calcium phosphates synthesized at low temperature, Acta Biomater 6 (6) (2010) 1882–1894.